PROCEEDINGS, 50th Workshop on Geothermal Reservoir Engineering
Stanford University, Stanford, California, February 10-12, 2025
SGP-TR-229

Fluid flow, Rock Deformation, and Seismic Response During Utah FORGE Circulation Tests

Ahmad Ghassemi, Zhi Ye*, Sang H. Lee, Jonathan Ajo-Franklin**

Reservoir Geomechanics and Seismicity Research Group, The University of Oklahoma, Norman, OK, USA

*South Dakota School of Mines & Technology, SD, USA

**Rice University, Houston, Texas, USA

ahmad.ghassemi@ou.edu

Keywords: Utah FORGE, EGS, Reservoir Simulation, Discrete Fracture Network, Kaiser Effect, Seismicity, Stress Shadow

ABSTRACT

In this work, we investigate the Utah FORGE circulation experiments conducted in 2023, within the stimulated reservoir volume (SRV) resulting from the multi-stage stimulation of April 2022. Using field data and modeling, we estimate the extent and permeability of the SRV by integrating micro-seismicity data and injection pressure records. Pore pressure mapping and flow distribution in the circulation tests are obtained as part of the modeling and calibration using field data. The analysis of micro-seismic record illustrates the geomechanical features of the reservoir rock mass response to stimulation, depicting the contributions of both hydraulic fracturing and shear stimulation mechanisms. Finally, phenomenon related to the onset of seismicity during fluid circulation is described and analyzed. Notably, our findings indicate a violation of the Kaiser effect during reinjection into previously stimulated SRV. Furthermore, pressure diffusion appears to be the more dominant driver of microseismicity in comparison to stress shadow and its relief.

1. INTRODUCTION

The Utah FORGE stimulation and circulation experiments have provided valuable data that can be used to analyze permeability and geomechanical aspects of the SRV formed during hydraulic stimulation. We previously analyzed the reservoir stimulation process and permeability structures during Stages 1-3 and Stage 3R (Lee and Ghassemi, 2022, 2023; Kumar and Ghassemi, 2023), which suggested that the propagation of hydraulic fractures likely interact with natural fractures, leading to a more complex SRV comprising a hydraulic fracture/natural fracture (HF/NF) network. In this work, we focus on circulation tests between the injection well 16A(78)-32 (or referred to as 16A) and the production well 16B(78)-32 (or referred to as 16B), the observed seismicity, and pressure changes around the fluid circulation zones to evaluate the geomechanical characteristics of the SRV. We present new observations on the fracturing processes, the pressure required for the onset of fracture deformation and induced seismicity in relation to the Kaiser effect. Additionally, we explore the potential contributions of stress shadow, pore pressure, and poroelastic stress to the recorded micro-seismicity. This analysis is conducted using 3D numerical simulations and analytical solutions, integrating various field data from Utah FORGE.

2. COMPLEX SRV CREATED BY STAGES 1-3 STIMULATION

In this section, we summarize some of our key modeling results of Stages 1-3 of the Utah FORGE stimulation, aiming to reveal the likely fracturing processes and SRV development (Kumar and Ghassemi, 2023). Our 3D numerical simulations considered the presence of natural fractures (NFs) in the FORGE reservoir, as suggested by the Utah FORGE Team's fitted planes based on log data, field observations, and recorded seismicity. These natural fractures have the potential to be reactivated during stimulation and fluid injection. Using Stage 3 as an example, the discrete fracture network (DFN) distribution around the wellbore applied in the hydraulic fracturing (HF) simulation is shown in Figure 1 (left). It is important to note that additional NFs were included (away from the wellbore) to ensure adequate leak-off, satisfying the mass balance requirements. A comparison between simulated pressure transients and actual field pressure records for the Stage 3 simulation is shown in Figure 1 (right), demonstrating good agreement.

The results of hydraulic fracture propagation and its interaction with natural fractures are shown in Figure 2 (left), while the field-recorded MEQ data is superimposed on the HF-NF networks in Figure 2 (right). The findings demonstrate a strong correlation between seismic activity and SRV development, suggesting a mixed-mode stimulation mechanism. Stage-3 stimulation likely involved the propagation of hydraulic fractures and their interaction with natural fractures, resulting in the reactivation of NFs and the formation of a complex SRV.

We reprocessed the microseismic data associated with the Stage-3 stimulation and mapped the seismic cloud, as shown in Figure 3. Within the microseismic cloud, a hydraulic fracture plane perpendicular to the wellbore, along with several natural fracture planes, can be visually identified and fitted. This observation aligns with our modeling results, which indicate that the SRV at the FORGE reservoir was created through hydraulic fracture propagation coupled with the reactivation of natural fractures. Notably, wing-crack propagation features are clearly observed within the microseismic cloud, providing strong evidence of mixed-mode stimulation. This behavior—involving hydraulic fracturing and shear stimulation of natural fractures—is consistent with field observations from previous EGS stimulations (e.g., Jung 2013) and laboratory experiments (Ye & Ghassemi, 2018, 2019). These results further support the conclusion that SRV creation at FORGE involves a combination of hydraulic fracturing and shear stimulation mechanisms.

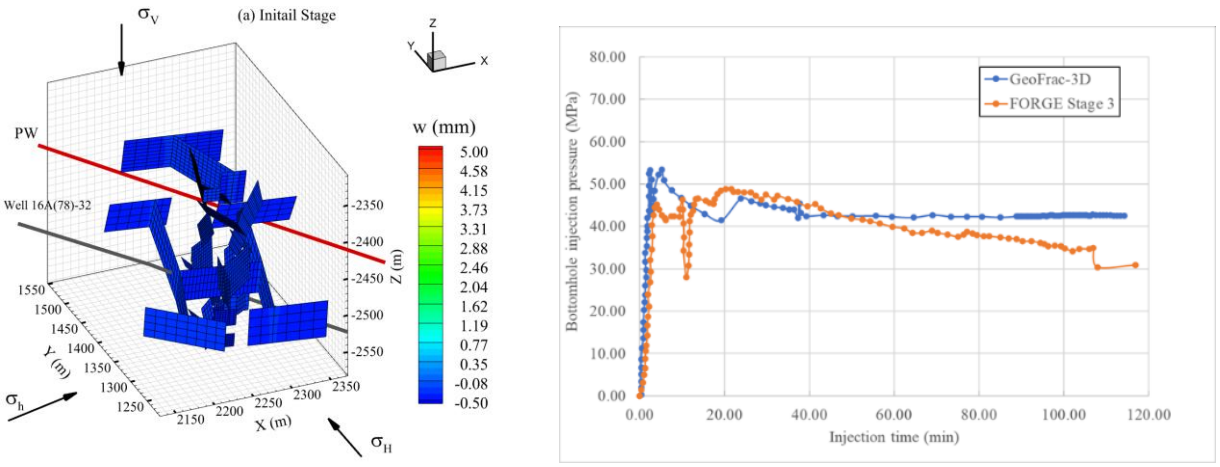

Figure 1: (Left) Discrete fracture network (DFN) used in the Stage 3 stimulation; (Right) Comparison of field pressure records with numerical simulation results.

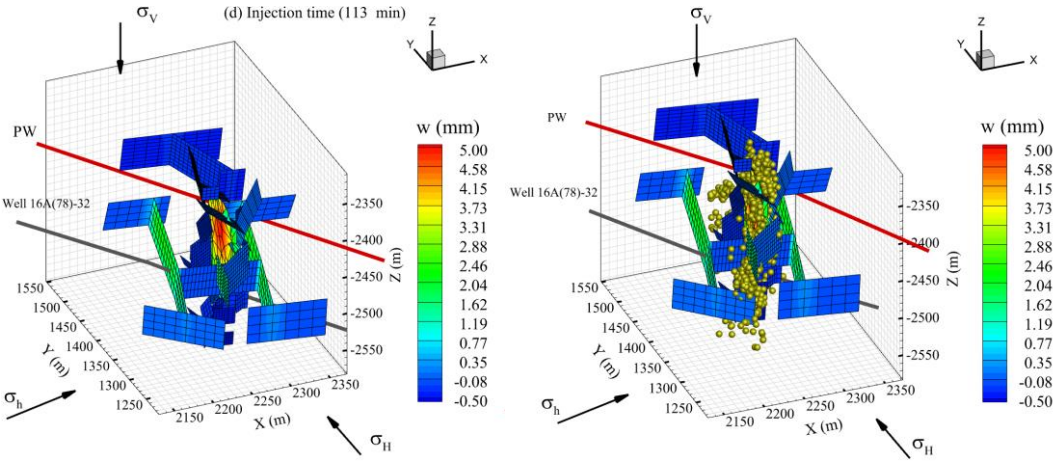

Figure 2: Numerical model results of hydraulic fracture growth. The right figure superimposes the seismicity data on the DFN and the HF.

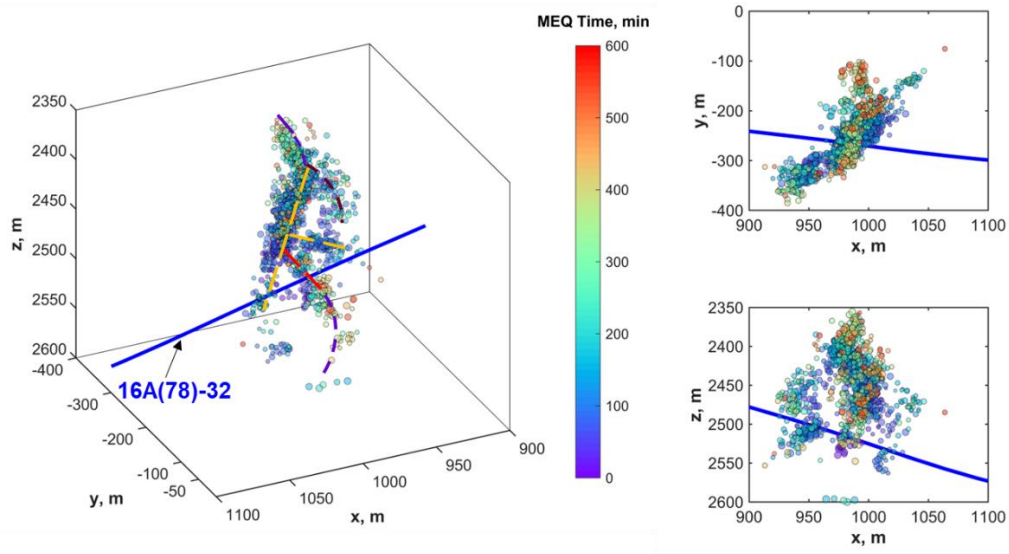

Figure 3: Microseismicity distribution of Stage-3 stimulation, with visually fitted hydraulic fracture (HF) and natural fracture (NF) planes overlaying the seismic cloud.

3. MODELING AND ANALYSIS OF UTAH FORGE CIRCULATION TESTS

Two sets of circulation tests, comprising a total of four tests, were conducted to evaluate interwell fluid flow and recovery. The first set, Circulation Test 1 (C1) and Circulation Test 2 (C2), was performed on July 4th and 5th, 2023, with Well 16B(78)-32 in an openhole condition. The second set, Circulation Test 3 (C3) and Circulation Test 4 (C4), was conducted from July 18th to 20th, 2023, with Well 16B(78)-32 in a cased-hole condition down to 10,208 ft MD, leaving 739 ft openhole below this depth.

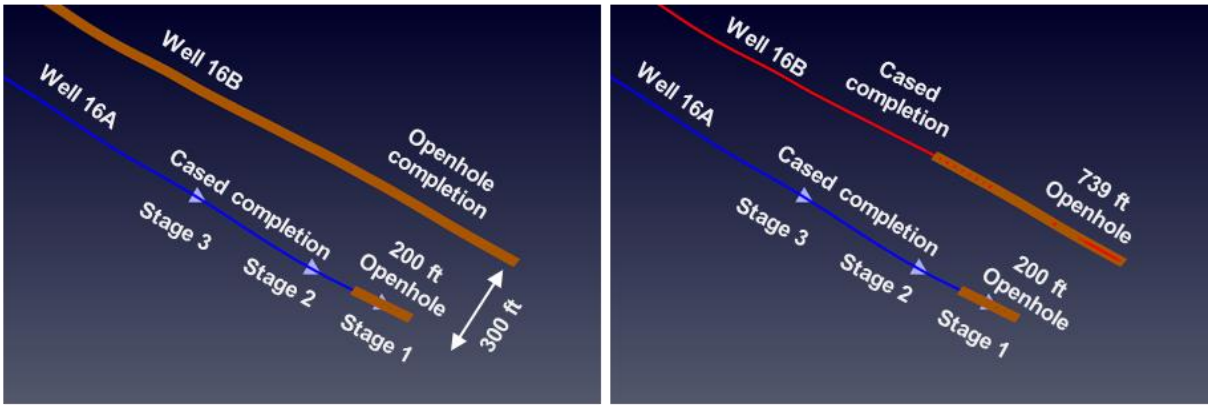

Figure 4: Overview of circulation tests conducted in Utah FORGE between Well 16A(78)-32 and Well 16B(78)-32. (Left) Circulation Test 1 (C1) and Circulation Test 1 (C2), performed on July 4th and 5th, 2023, with Well 16B(78)-32 in an openhole condition. (Right) Circulation Test 2 (C3) and Circulation Test 1 (C4), conducted from July 18th to 20th, 2023, with Well 16B(78)-32 in a cased-hole condition to 10,208 ft MD, and 739 ft openhole below this depth.

The simulations of the circulation tests incorporate the equivalent permeability derived from the discrete fracture network (DFN) and the hydraulic fractures (HF) created during Stage 1-3 stimulation. Permeability variations in response to induced pressure and temperature changes are also accounted for. The size of the SRV is constrained by the extent of the microseismicity data around Stage 1, 2, 3. For the wellbore grid-blocks, the model uses an ultra-high permeability (10^6 Darcy), and an ultra-low permeability (10^{-9} md) to simulate the cased hole walls. It is observed that the stimulated volumes are overestimated if we include all seismic events, so we filtered out several outliers during the calibration work as described in Figure 5. The input parameters used for simulations are listed in Table 1. Aside from its permeability, the reservoir state is assumed to be the native state i.e., temperature and pore pressure disturbance during drilling and other activities have dissipated.

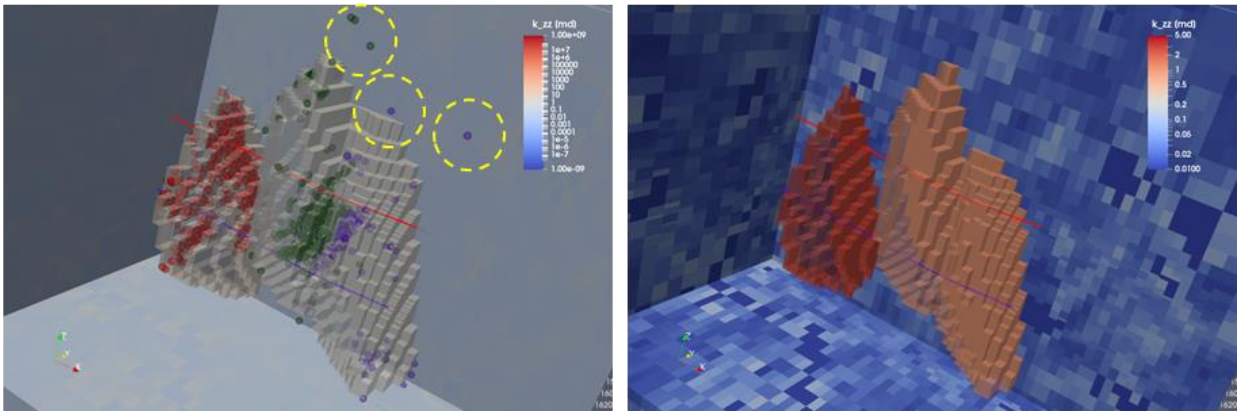

Figure 5: (a) Microseismic events data and stimulated volume. The outliers are marked as yellow circles and filtered out during the calibration work to improve the results. (b) DFN permeability distribution and high permeability zones around Stage 1, 2, 3.

Table 1: Input parameters for modeling Utah FORGE Circulation Tests

Parameter	Value
Porosity, Ø	1 %
Thermal conductivity,	4.0 W/m-K
Matrix permeability, *K*	DFN upscaled permeability
Heat Capacity	1200 J/Kg-K

Density of rock	2.7 g/cm^3
Residual water saturation	0.30
Residual steam saturation	0.05

3.1 Numerical Modeling for Circulation Tests C1 and C2

The injection well 16A(78)-32 was drilled and cased in 2021, with a 200 ft openhole section below 10,787 ft MD, and subsequently stimulated in April 2022. The first set of circulation tests, Circulation Test 1 (C1) and Circulation Test 2 (C2), were conducted on July 4th and 5th, 2023. At that time, the production well 16B(78)-32 was cased using an 11.75-inch with the casing shoe at 4,837 ft MD, leaving 6,110 ft of openhole below this depth. The wellhead pressure and injection rates of C1 used for calibration of the model (the injection rate and wellhead pressure in Well 16A(78)-32, and the wellhead pressure in the production Well 16B(78)-32) are presented in Figure 6. The modeling result for permeability changes with respect to the injection rate in C1 are plotted in Figure 7. We calibrate the permeability based on the pressure response to a prescribed injection rate. It is observed that both pressure and permeability increased as the injection rate increases. The pressure initially increases and then decreases slowly after 500 min because of the fracture reopening, and this is interpreted as permeability increases as plotted in Figure 7(a) and (b). Additionally, the pressure of Well 16B(78)-32 increases as the fluid was injected into the Well 16A(78)-32. Consistent with the field data, a fixed pressure condition is applied after 500 min of circulation. Details of the permeability structure used, and their values obtained for calibration can be found in Lee and Ghassemi (2022; 2023). However, it is worth noting that the calibrated permeability from circulation modeling is lower than that from stimulation modeling, which aligns with the lower injection rates used in the circulation tests. Reservoir pressure variations during Circulation Test 1 (C1) are presented in Figure 8. The pressure changes are more localized around the injection zones in the early stages and dissipate slowly as the injection rate decreases.

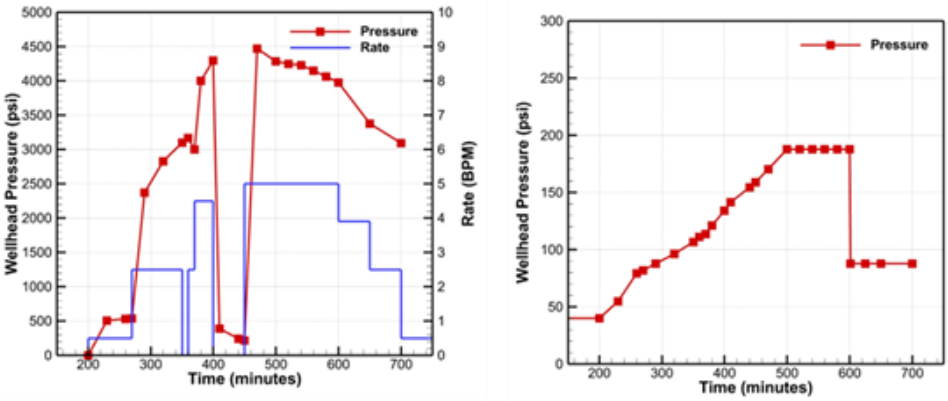

Figure 6: Modeling input from the field data for Circulation Test 1 (C1). (Left) injection rate and wellhead pressure at 16A(78)-32; (right) wellhead pressure at well 16B(78)-32. Pressure boundary conditions are applied after 500 minutes, as indicated by field data, to maintain the pressure limit in Well 16B(78)-32.

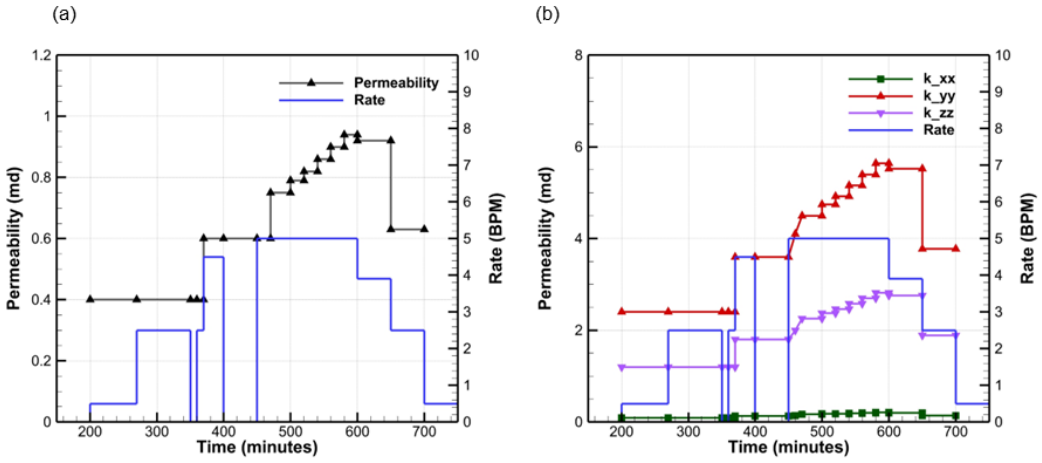

Figure 7: Permeability modeling results for the first Circulation Test 1 (C1) are plotted. (Left) Permeability model around Stage1 and 2. The isotropic permeability model has been implemented to match the isotropic microseismic events clouds. The permeability ranges from 0.40 md to 0.94 md. (Right) Permeability model around Stage 3. The anisotropic permeability model has been implemented to match the anisotropic microseismic events cloud. The calibrated anisotropic permeability for k_{xx} = 0.09 – 0.21 md, k_{yy} = 2.40 – 5.64 md, k_{zz} = 1.20 – 2.82 md.

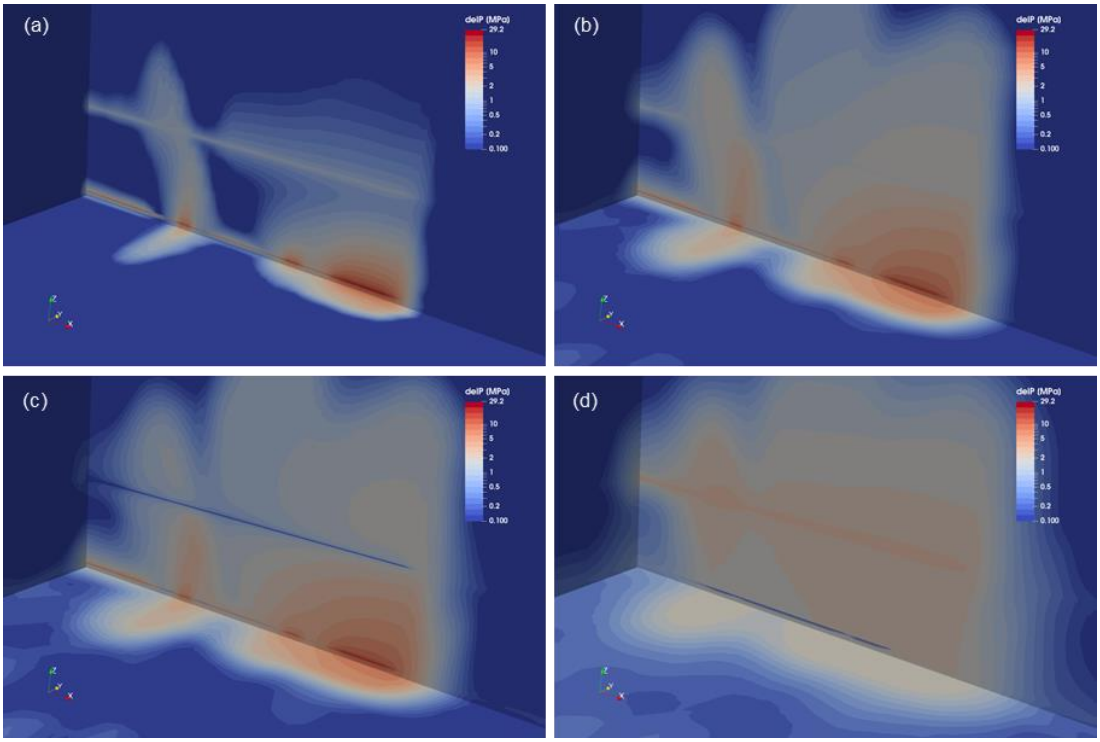

Figure 8: The change of pressure distributions for the Circulation Test 1 (C1) are plotted. (a) t = 270 min, (b) t = 350 min, (c) t = 470 min, (d) t = 700 min. A fine grid blocks is used in all simulations (0.22 m vs 10 m regular grid-block for stimulation modeling of Lee and Ghassemi, 2022).

For Circulation Test 2 (C2), an injection rate of 5.0 BPM was used for 400 min while the production Well 16B(78)-32 pressure was held at 200 psi for 300 min, and then the pressure was controlled stepwise up to 500 psi from 400 min to 950 min. The numerical model was developed to replicate field test conditions. The numerical pressure predictions for the injection well with 5.0 BPM injection rate is presented in Figure 9 (left). The pressure boundary conditions for the production well and the corresponding flow rates at different time-steps are also plotted in Figure 9 (right). It was observed that the pressure increased rapidly for the first 50 min in the injection well and then decreased slowly until the end of circulation test. The pressure behavior for a constant rate injection indicates that hydraulic/natural fractures were likely reactivated during the circulation test. The calibrated permeability shows gradual increase in all 3 stimulation stages as plotted in Figure 10. The permeability ranges from 0.55 md to 0.98 md for Stage 1 and 2, and kxx =0.11 – 0.22 md, kyy =3.00 – 5.88 md, kzz =1.50 – 2.94 md for Stage 3. 3D plots for pressure changes in the reservoir at different time-steps are presented in Figure 11. Similar to the observations in C1, the pressure changes were more localized around the injection zones in the early stages and dissipated gradually as the injection rate decreased.

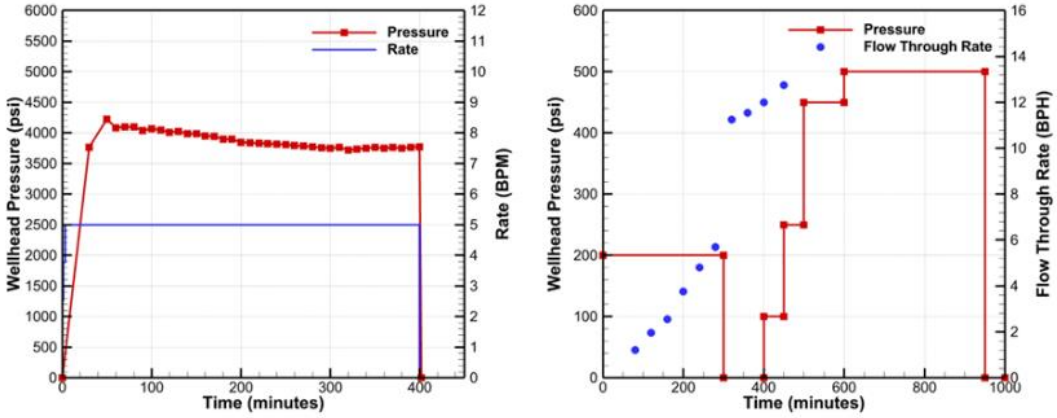

Figure 9: Pressure modeling results for Circulation Test 2 (C2) are plotted. (Left) model calibration for Well 16A(78)-32 based on the injection rate and pressure response; (Right) calibration for Well 16B(78)-32. Pressure boundary conditions are applied after 500 min as indicated by field data (hold 16B pressure limit). The flow through rate for Well 16B(78)-32 is also plotted with blue dots.

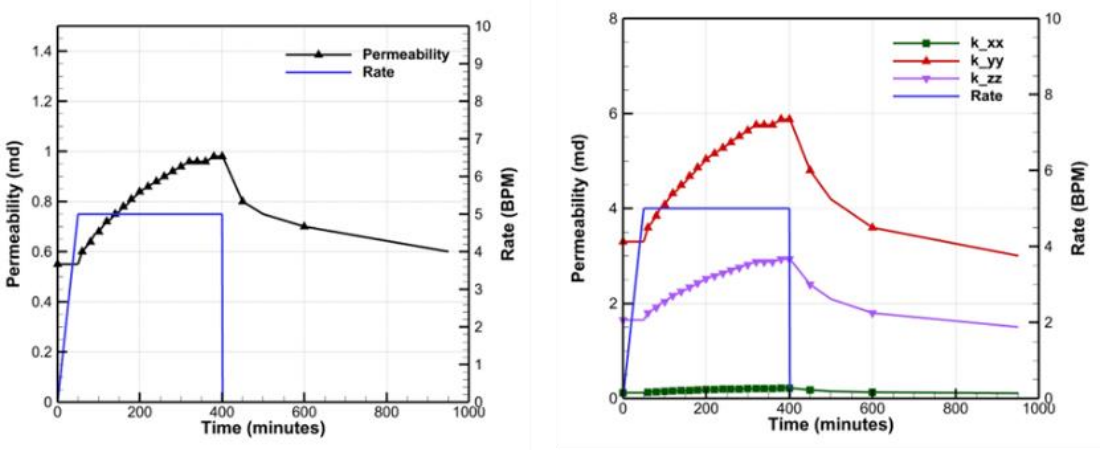

Figure 10: Permeability modeling results for Circulation Test 2 (C2) are plotted. (Left) Permeability model around Stage1 and 2. The isotropic permeability model has been implemented to match the isotropic microseismic events clouds. The permeability ranges from 0.55 md to 0.98 md. (Right) Permeability model around Stage 3. The anisotropic permeability model has been implemented to match the anisotropic microseismic events cloud. The calibrated anisotropic permeability for k_{xx} = 0.11 – 0.22 md, k_{yy} = 3.00 – 5.88 md, k_{zz} = 1.50 – 2.94 md.

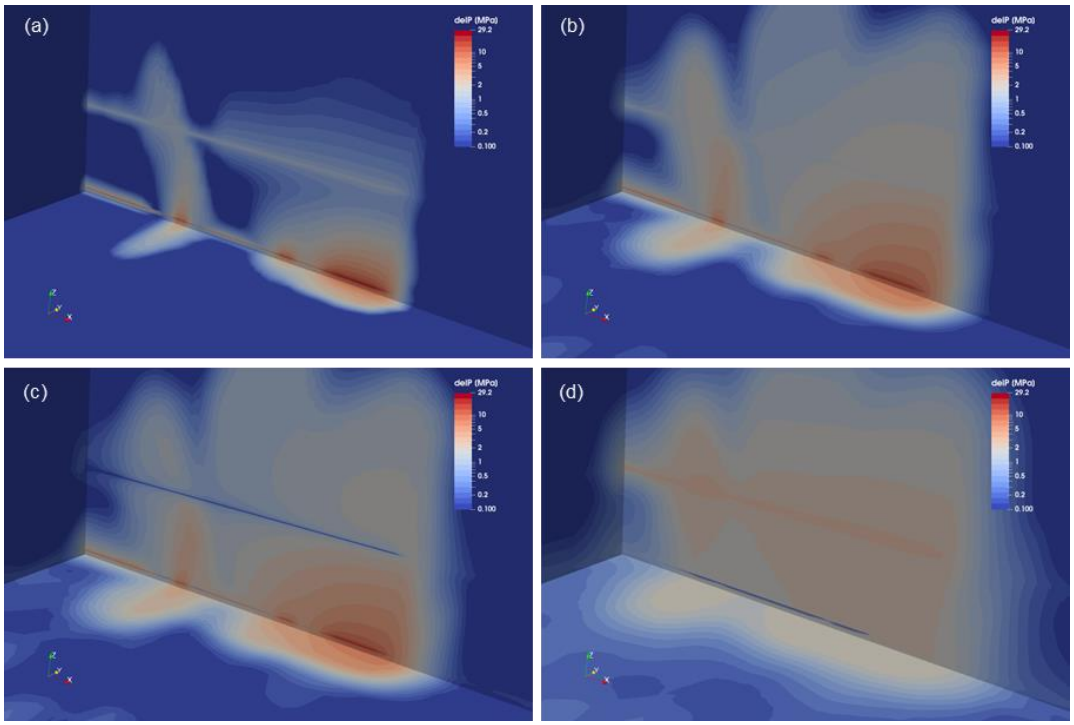

Figure 11: The temporal changes of pressure distributions for Circulation Test 2 (C2) are plotted. (a) t = 50 min, (b) t = 300 min, (c) t = 400 min, (d) t = 950 min.

3.2 Numerical Modeling for Circulation Tests C3 and C4

Following the two circulation tests in July 4th and 5th, 2023 (Circulation Test 1 and Circulation Test 2), Well 16B(78)-32 was cased to 10,208 ft, MD as described in Figure 12 (b). The second set of circulation tests, Circulation Tests 3 (C3) and Circulation Tests 4 (C4), were performed between July 18th and July 20th, 2023. In these tests, the maximum injection rate was increased up to 7.5 BPM compared to the 5.0 BPM used in the C1 and C2. In the simulations, we use an ultra-low permeability value of 10^{-9} md around the production wellbore, while allowing for openhole conditions below 10,208 ft, MD. Pressure modeling for Circulation Test 3 (C3) is plotted in Figure 12 (b) and the permeability model calibrations for Stage 1, 2, 3 are plotted in Figure 13. The numerical model results for pressure changes are presented in Figure 14.

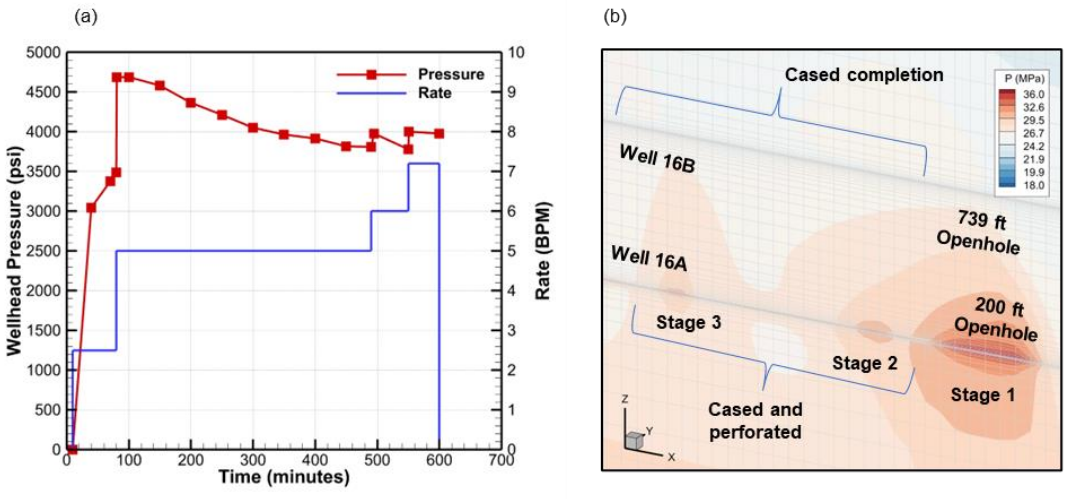

Figure 12: Pressure modeling results for Circulation Test 3 (C3) are plotted in (left), and the cross-sectional view around circulation zones including the irregular grid-blocks is presented in (Right).

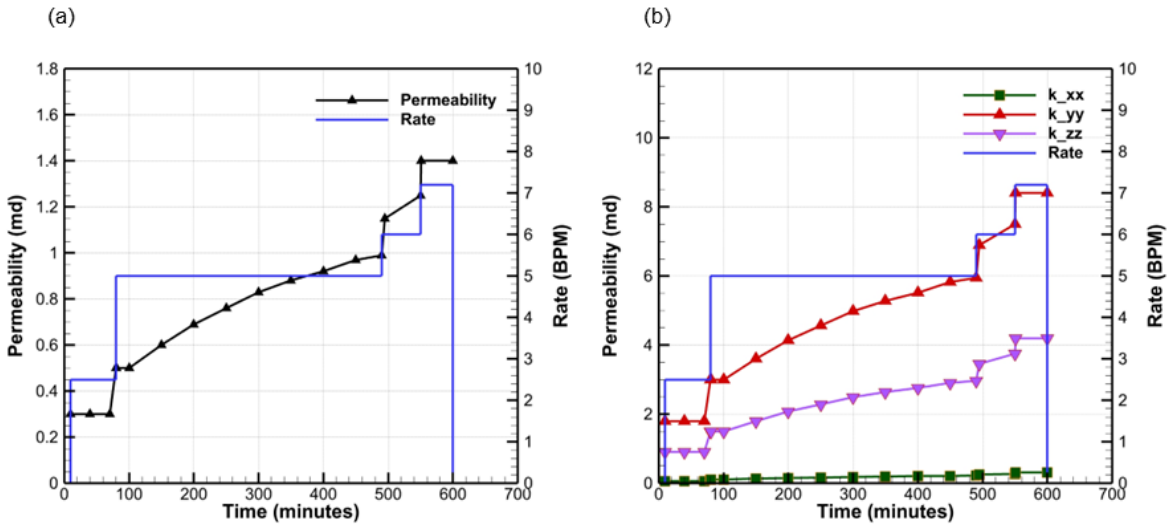

Figure 13: Permeability modeling results for Circulation Test 3 (C3) are plotted. (a) Permeability model around Stage1 and 2. The isotropic permeability model has been implemented to match the isotropic microseismic events clouds. The permeability ranges from 0.30 md to 1.40 md. (b) Permeability model around Stage 3. The anisotropic permeability model has been implemented to match the anisotropic microseismic events cloud. The calibrated anisotropic permeability for k_{xx} = 0.07 – 0.31 md, k_{yy} = 1.80 – 8.40 md, k_{zz} = 0.90 – 4.20 md.

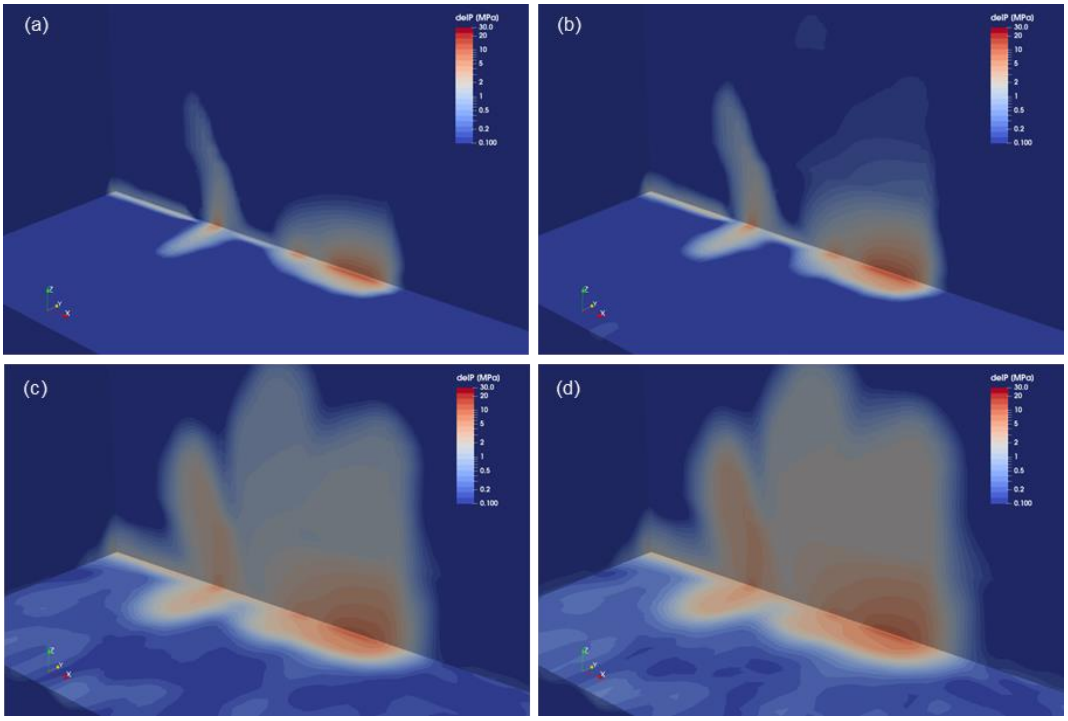

Figure 14: The temporal changes of pressure distributions for Circulation Test 3 (C3) are plotted. (a) t = 70 min, (b) t = 120 min, (c) t = 420 min, (d) t = 590 min.

For Circulation Test 4 (C4), the injection rate was stepwise increased from 2.5 BPM to 7.5 BPM. As shown in Figure 15(a), the pressure response to the injection rate is consistent to the patterns observed in other Circulation Tests (C1, C2, and C3), and the calibrated permeability model also produced similar values as illustrated in Figure 16. Permeability values range from 0.28 md to 1.37 md for Stage 1 and 2, and for Stage 3, they were k_{xx} = 0.06–0.30 md, k_{yy} = 1.68–8.22 md, and k_{zz} = 0.84–4.11 md. Spinner data measured on July 19th, 2023, indicates a flow partition of 44 – 50 % into Stage 1, and 30 – 40% into Stage 3. Our numerical modeling results on fractional flow rates, Shown in Figure 15(b), align well with the spinner measurements. The data reveals distinct trends in fractional flow rate variations with respect to different circulation rates. For Stage 1, the fractional flow rate decreases as the circulation rate increases. Conversely, for Stage 3, the fractional flow rate increases with higher circulation rates. The fractional flow rate is increased as the circulation rate is increased for Stage 3. This variability highlights the complexity of rock permeability around different stimulation zones, which involves the interaction of natural fractures and hydraulic fractures between the injector and the producer, complicating interpretations. The observed phenomenon can likely be attributed to more favorable fracture orientations in Stage 3, which open in response to increased injection rates. In contrast, Stage 1 is likely dominated by pre-existing natural fracture permeability that require higher pressures than S3 to reopen.

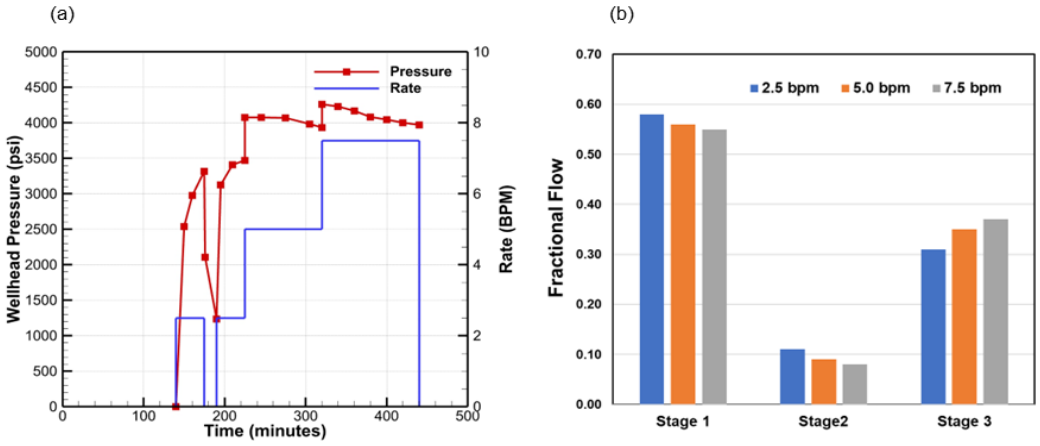

Figure 15: Pressure modeling results for Circulation Test 4 (C4) are plotted in (a), and the fractional flow rate modeling for different injection rates is presented in (b).

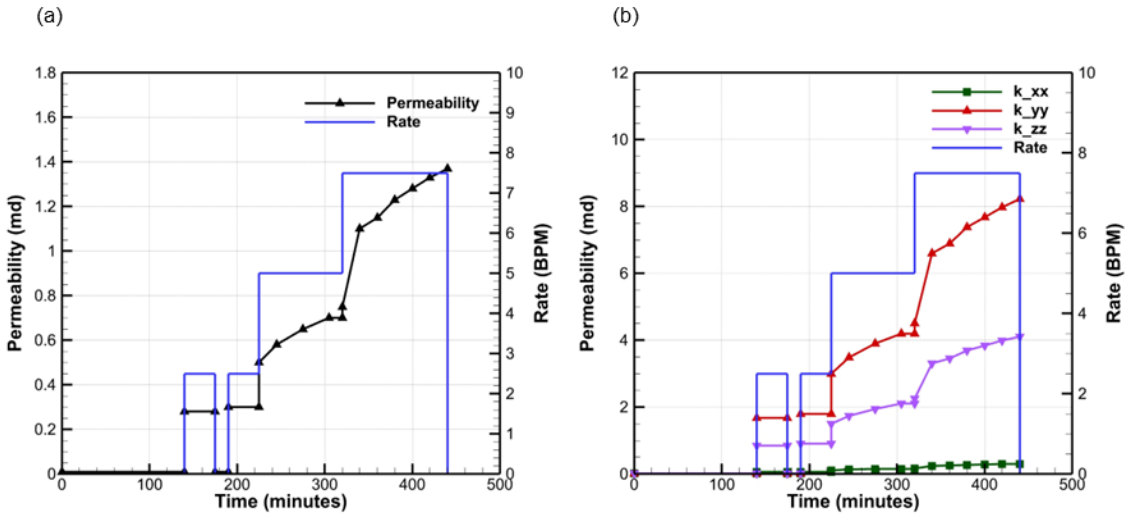

Figure 16: Permeability modeling results for the second Circulation Test 4 (C4) are plotted. (a) Permeability model around Stage1 and 2. The isotropic permeability model has been implemented to match the isotropic microseismic events clouds. The permeability ranges from 0.28 md to 1.37 md. (b) Permeability model around Stage 3. The anisotropic permeability model has been implemented to match the anisotropic microseismic events cloud. The calibrated anisotropic permeability for k_{xx} = 0.06 – 0.30 md, k_{yy} = 1.68 – 8.22 md, k_{zz} = 0.84 – 4.11 md.

The 3D numerical results at different times are illustrated in Figure 17 and Figure 18. Similar to other circulation test results, the pressure diffusion pattern indicates insufficient connection between the injector and the producer. Therefore, further stimulation of the injector, the producer, or both would be necessary to improve connectivity. The numerical results also provide the fractional flow rates for each stage around the injector Well 16A(78)-32, as shown in Figure 19 (Left). It is observed that the numerical results differ from field data by 5-10% (Figure 19 (right)). However, the overall trend of fractional flow rate variations with respect to the injection rate from numerical modeling are in very good agreement with field observations.

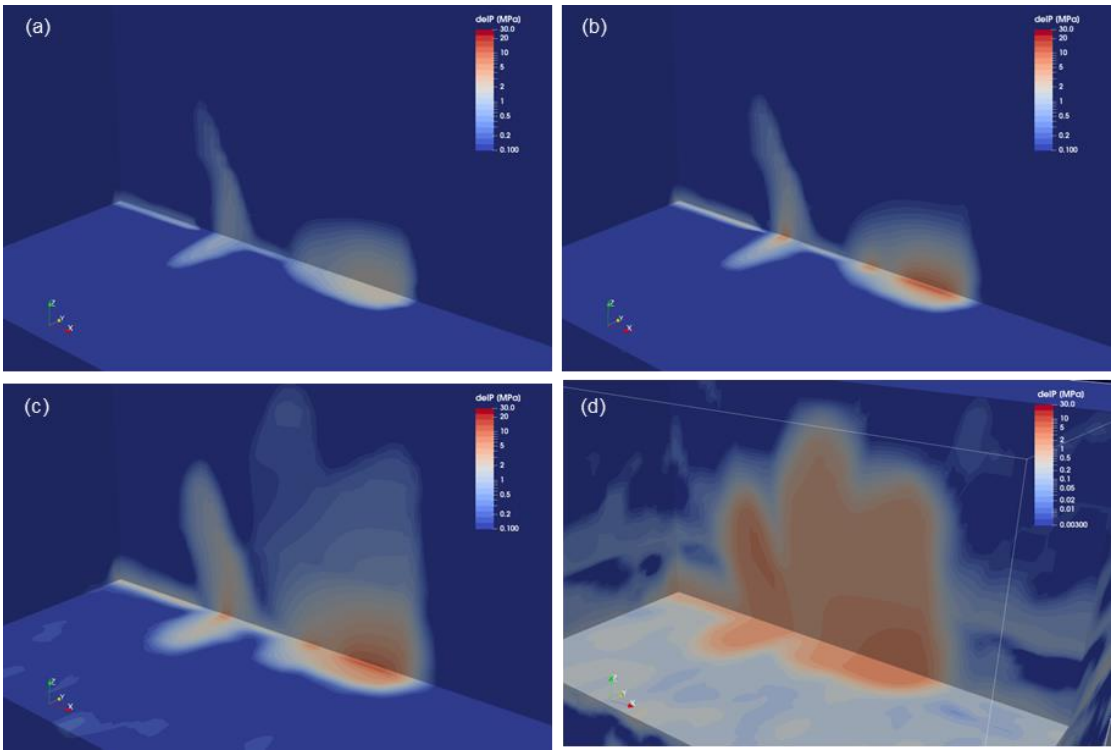

Figure 17: The change of pressure distributions for the second Circulation Test 4 (C4) are plotted. (a) t = 190 min, (b) t = 225 min, (c) t = 320 min, (d) t = 500 min.

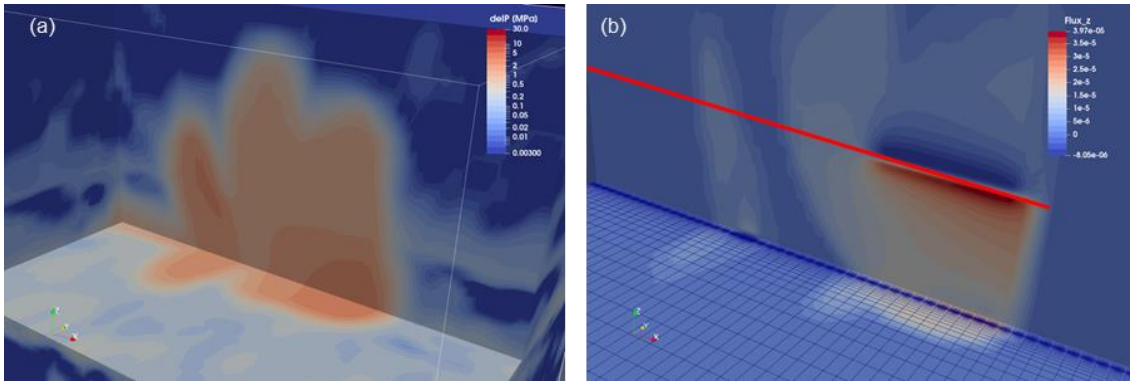

Figure 18: The change of pressure and the flux distribution for the second Circulation Test2 (C4) are plotted. (a) pressure change at t = 500 min and (b) volume flux distribution at t = 500 min.

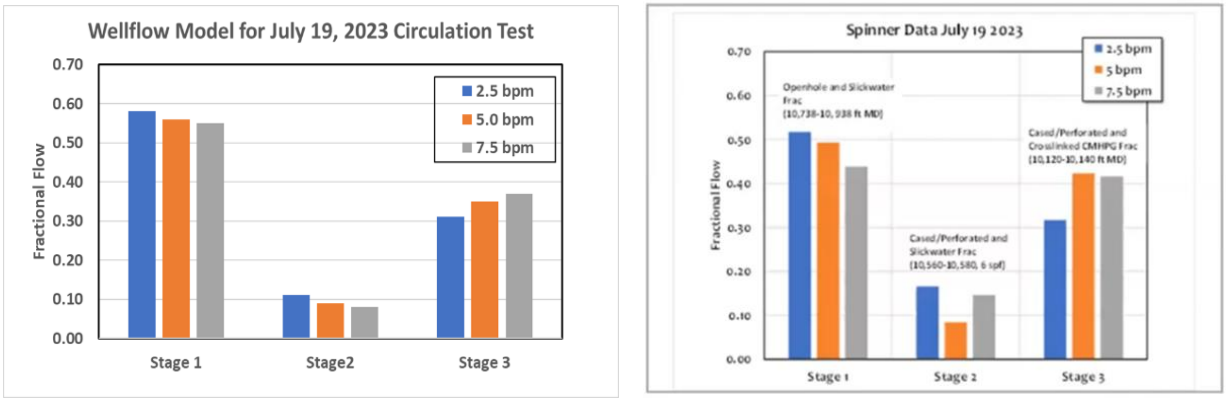

Figure 17: The fractional flow rate modeling for different injection rates and observed flow in the well (b).

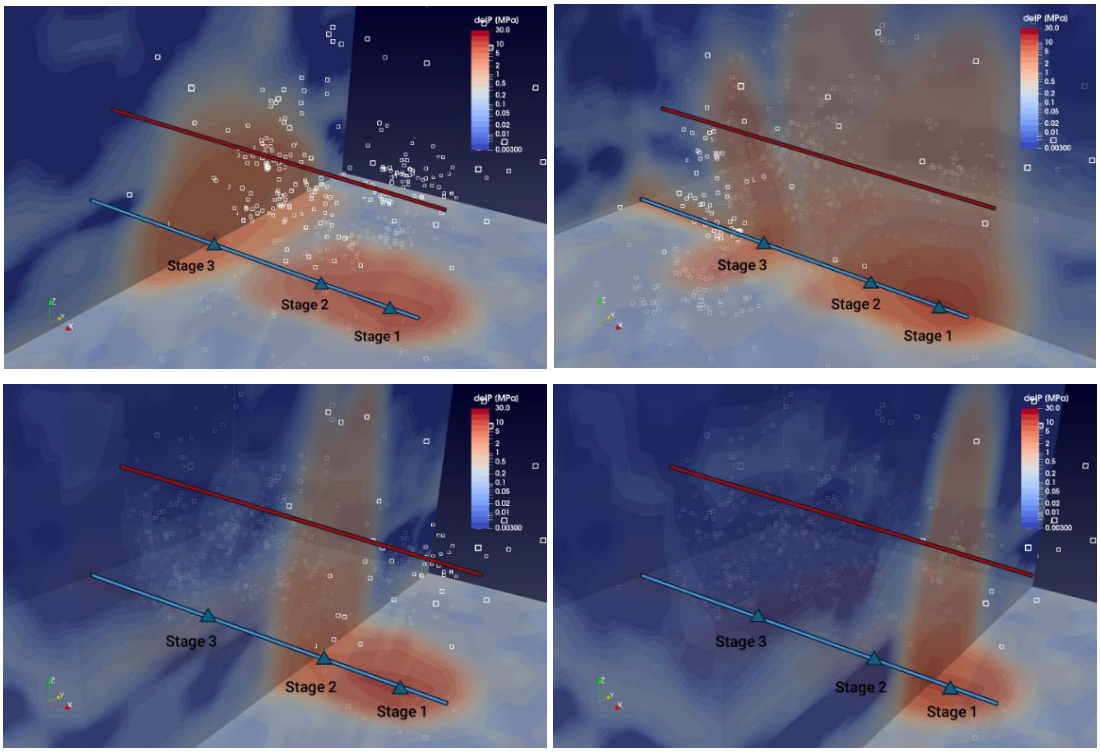

Figure 18: Visualization of microseismic activity data superimposed on the numerically modeled pressure field at 440 minutes into Circulation Test 4 (C4).

4. INTERPRETATION OF MICROSEISIMITY DURING CIRCULATION TESTS 1-4

4.1 Heterogeneous Seismicity Distribution

The microseismic data recorded during the circulation tests has been reported by the Utah FORGE (GDR; Niemz et al., 2024). This dataset is based on permanent surface monitoring stations that recorded 962 events for the 2023 circulation tests. For a detailed discussion of seismicity monitoring, interpretation methods, and data quality, refer to Niemz et al. (2024). Figure 20 shows the microseismic data superimposed on the numerically determined pressure field at 440 min, corresponding to the end of Circulation Test 4 (C4) during the second set of circulation tests conducted from July 18th to July 20th, 2023.

As indicated by spinner measurements in Figure 17 (Right), 50% or more of the pumped fluid was absorbed by Stage 1 zone, approximately 40% entered the Stage 3 zone, and the remainder was taken up by Stage 2 zone. However, Stages 1 and 2 exhibited significantly less microseismic activity, while the majority of the microseismic events were concentrated around Stage 3 zone. This observation is further illustrated in Figure 21, which shows the microseismic data recorded during Circulation Test2 (C2) superimposed on the data from stimulation stages S1-S3. Most events were localized around the Stage 3 SRV or fracture planes, with considerably fewer microseismic events scattered around the SRV of Stages 1-2. This pattern is nearly the same during the second set of circulation tests, C3 and C4, as shown in Figure 22.

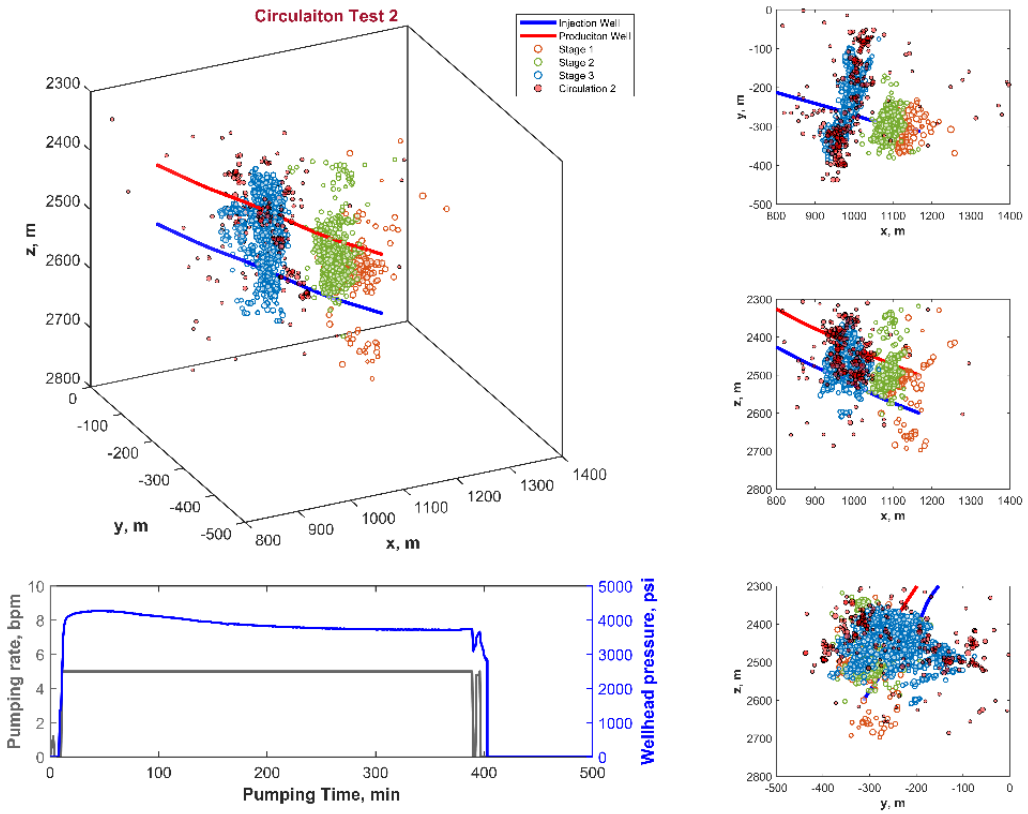

Figure 19: Superposition of microseismic events recorded during Circulation Test 2 (C2) on the microseismic data from Stages 1–3 stimulation. Results indicate that the majority of micro seismicity during circulation concentrated in Stage 3 SRV.

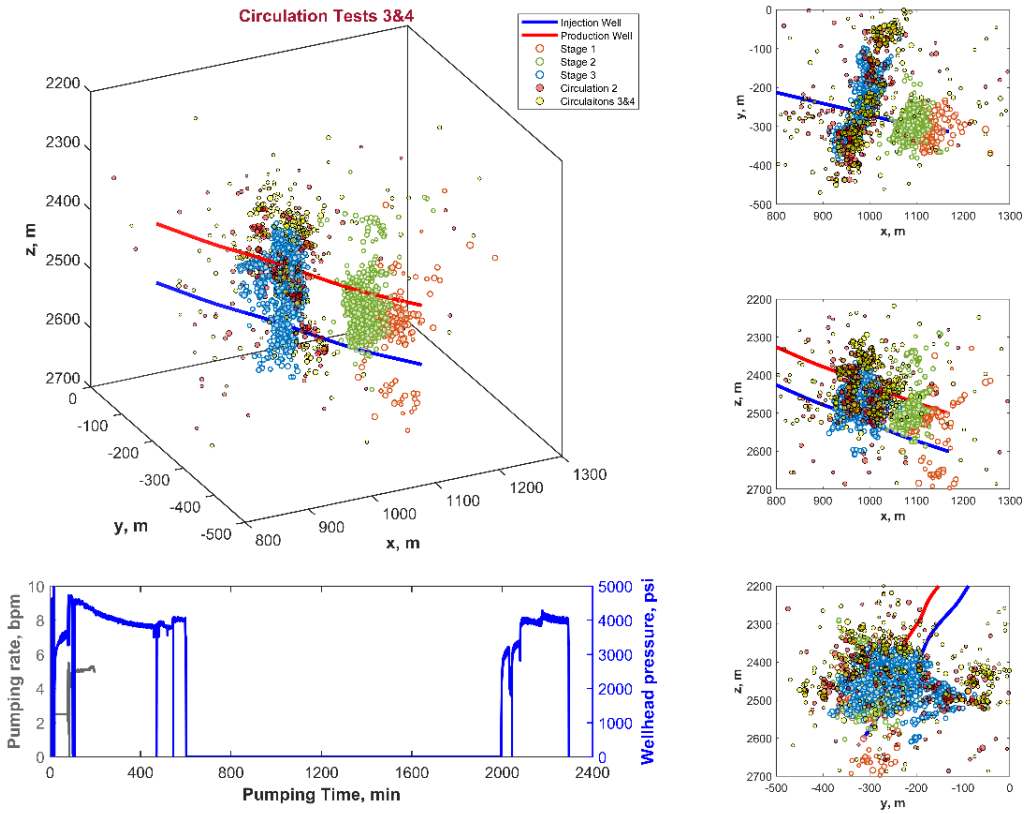

Figure 20: Superposition of microseismic events recorded during Circulation Tests 3 and 4 (C3 and C4) on the microseismic data from Stages 1–3 stimulation and Circulation Test 2 (C2). Results indicate that the majority of microsiemsicity during circulations concentrated in Stage 3 SRV.

This is a clear indication that MEQ activity corresponds primarily to zones experiencing pressure increases rather than fluid flow. This observation is consistent with Niemz et al. (2024), citing Cornet et al. (1997), who suggested an aseismic zone in the SRVs of Stage 1 (S1) and Stage 2 (S2). However, according to our simulations, all 3 zones experienced similar pressure changes. So, the lack of seismicity in stage 1 and 2 is enigmatic. We attribute this to the unfavorable orientation of natural fractures in these stages, combined with their cohesive strength, which requires higher pressure for reactivation.

In contrast, the higher concentration of MEQs in the SRV of Stage 3 (S3) suggests that the fractures in this zone are more favorably oriented, allowing for larger shear displacements and dilation in response to increased injection rates, which triggers more seismic events. Stages 1 and 2, on the other hand, are likely dominated by pre-existing natural fractures with unfavorable orientations. While these fractures readily accept fluid due to their high permeability, they do not generate significant shear displacements, as reflected by the fewer scattered microseismic events around their SRV.

Stimulation data (field notes), microseismic activity, and flow distribution seem to suggest the SRVs of S1 and S2 are hydraulically connected, with a higher density of natural fractures that are likely already open or were opened or dilated during stimulation of S1 and S2. Therefore, fluid can enter these relatively higher permeability zones without causing microseismicity. Additionally, the pressure profiles of S1 and S2 do not exhibit characteristics of classical hydraulic fracture initiation and propagation. It is more likely that these zones, selected for their higher occurrence of unfavorably oriented natural fractures, were primarily reactivated via shear and dilation during fluid injection. However, localized shear displacements in these zones did not coalesce into larger shear displacements along favorable orientations. Consequently, MEQ activity in the SRVs of S1 and S2 is relatively sparse, scattered, and locally distributed, without forming concentrated seismic clouds or planes, as shown in Figures 21 and 22.

In contrast, the pressure record of Stage 3 (S3) displays features that suggest mode 1 fracture propagation along a somewhat well-defined plane, at least for part of the time. Simulations considering the presence of natural fractures suggest that such a HF would have to intersect some preexisting natural fractures, possibly crossing them and in some cases reactivating them as it grows upward towards 16B. The treatment pressure for S3 is initially much higher than the minimum in-situ stress, indicating a complex hydraulic fracture network and/or near wellbore and/or far-field complexity (e.g., vertical segmentation) that results in significant tortuosity. The choke points tend to require higher pressure to open to allow fluid flow. While the treatment pressure does decline with continued pumping with fracture extension/volume availability; however, the pressure is comparable to that of S1 after about 80 min, even though the pumping rate is 30% lower. At low injection rates during stimulation, S1 treatment pressure is lower than S3 by 2-3 MPa, indicating S3 requires a higher

pressure compared to S1 for maintaining fluid flow at equivalent injection rates. Additionally, the fractional flow into S3 increases with an increase in the circulation pumping rate from 2.5 to 7.5 bpm. This trend can be explained by considering that the SRV of S1 and S2 are first filled during early pumping and the pressure needed to extend the less favorably oriented fractures within them is higher than that required for reopening and extending S3. Therefore, with higher circulation rates, flow into S3 increases to some extent.

The pressure, injection rate, and seismicity distributions as a function of time are shown in Figure 23-24 for C1-C4. As can be seen in Figures 23, during C1 the pressure increases with injection and rapidly drops after reaching ~4800 psi (8310 psi downhole), suggesting availability of new volume for water to flow into. However, no seismic activity is observed based on the available data. DFN data and equivalent permeability reservoir simulation indicate a high potential for fluid to flow into zone 1 (the SRVs around S1 and S2) without fracture propagation or significant hydroshearing. The pressure increase, coupled with the absence of microseismicty, indicates lack of criticality within zone 1, suggesting a relatively permeable near wellbore region (DFN) that potentially terminates against unfavorably stressed natural fracturs. These fractures would require much higher pressure to generate seismicity. In other words, zone 1 is not very seismic since it is already naturally fractured (DFN) and the fractures are not critically stressed. The open natural fractures take the injected fluid without significantly inflating or slipping. Notably, the injection pressure (at wellhead) is low, around 4800 psi (or 33 MPa). This has two implications: a) zone 1 likely needs to be mostly filled first, during which there is not much MEQ activity (actually, zone 1 never displayed much MEQ during previous stimulation treatment, possibly because the pressures were too low to induce seismicity in the rock mass); and b) The pressure during Circulation Test 1 (C1) is lower than pressures recorded during the previous stimulation, suggesting that the onset of any seismicity (even if not recorded) would likely occur at a lower pressure.

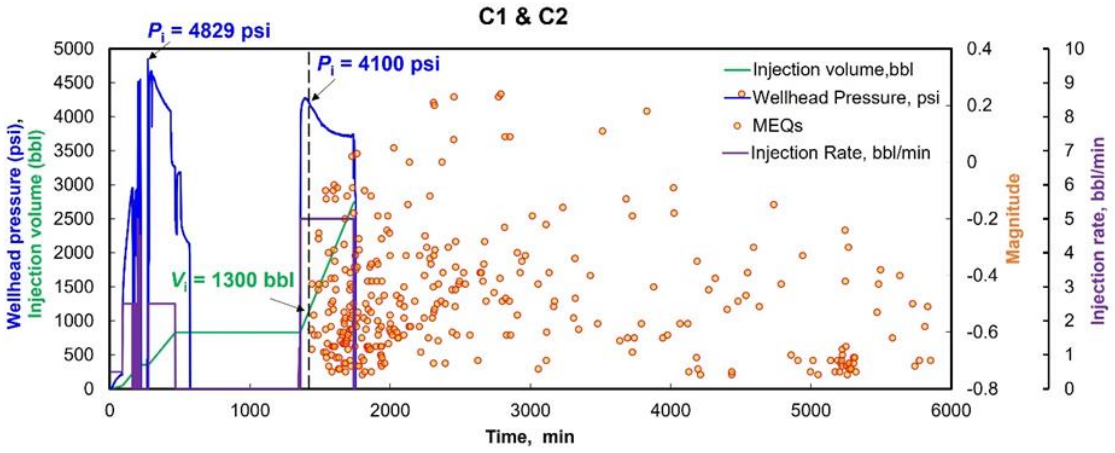

Figure 21: The temporal history of injection pressure, injection rate, total injection volume, and MEQ activities during the first set of circulation tests (C1 and C2).

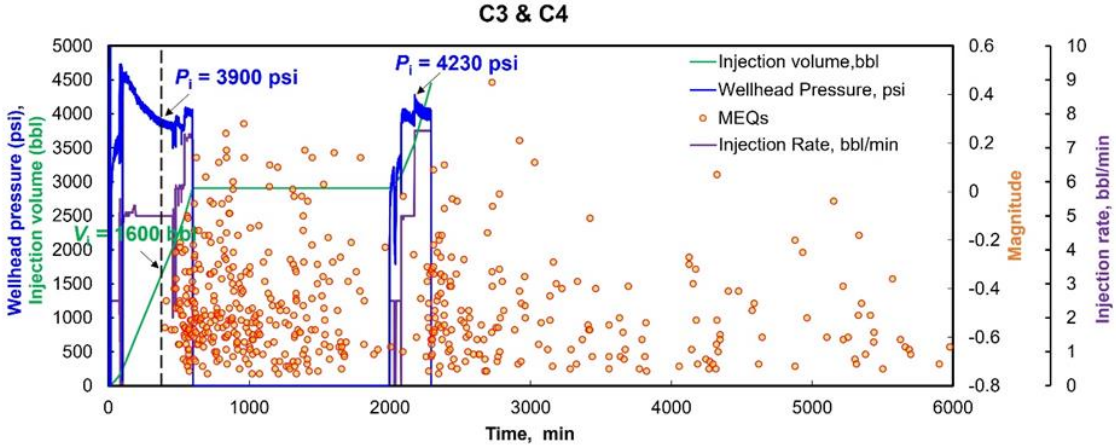

Figure 22: The temporal history of injection pressure, injection rate, total injection volume, and MEQ activities during the second set of circulation tests (C3 and C4).

4.2 Stress and Pore Pressure Criticality

The wellhead pressure in production well 16B increased during the second set of circulation tests (C3 and C4) with borehole cased in 16B. This suggests that the primary path of pressure communication between 16A and 16B is through the SRVs of S1 and S2, extending into the openhole toe section (see simulations). Field data shows pressure spikes of 1-3 MPa in 16B, and reservoir modeling of circulation

tests presented above shows approximately the same Δp values in 16B. Numerical simulations show the edge of the Δp dome, where microseismicity occurred when Δp has a value of roughly 2-3 MPa. This implies that a pressure of 28 MPa (2 MPa+26 MPa reservoir pressure) or 4060 psi is required for the onset of micro-seismicity on the periphery of the S3 SRV. This critical pore pressure is significantly below the S_{hmin} of 5867 psi (estimated at depth along the edges of the circulation seismicity zone). Consequently, the events are more likely caused by shearing of natural features and or strands of the hydraulic fracture that were formed during S3, rather than propagation of opening mode hydraulic fractures. The fact that circulation-induced seismicity (based on surface monitoring stations) nearly falls on noncoplanar offshoots of S_3 HF (Figure 3) supports this suggestion. Actually, this observation also underscores the notion that pressurization, rather than fluid flow, primarily leads to seismicity (Cornet, 1997). Furthermore, it shows that diffusion-driven reservoir pressure perturbations during C1-C4, which are significantly smaller than those during S1-S3, are responsible for the observed induced seismicity during circulation.

4.3 Violation of the Kaiser effect

The injection data shows that the onset of seismicity coincides with the intake of 1300-1600 bbls of fluid and at a wellhead pressure of 39-40 MPa, as illustrated in Figures 23 and 24. Niemz et al. (2024) provided a detailed analysis of the data and the pattern of seismicity. It has been suggested that the onset of seismicity during pumping cycles is consistent with the Kaiser effect. In this work, we propose an alternative explanation, that the data supports the notion that the Kaiser effect is violated in the circulation experiments.

In both sets of circulation tests, the seismicity begins before shut-in and at pressures below the previously recorded pressures during stimulation. As illustrated in Figure 25, the wellhead pressure at the onset of microseimsicity during Stage 3 is about 6236 psi. In contrast, the wellhead pressure at the onset of microseimsicity in both sets of circulation tests (Figure 23 and Figure 24) are significantly lower. Additionally, the pressures at onset of seismicity during C3 (~3900 psi) generally follow a decreasing trend compared to C2 (~4100 psi) and are certainly lower than the pressures during stimulation. Note that even in C4, the seismic activity starts before the pressure is elevated back to the C3 level. This phenomenon, noted by Shapiro et al. in the case of Barnett shale, suggests a violation of the Kaiser effect in the Utah FORGE SRV pressurization. The departure from the Kaiser effect is caused by the complexity of the rock structure near the S3 hydraulic fracture and associated shear stimulated zones, which react to the onset of pressurization and dilation of the main fractures at pressure lower than during the stimulation (Shapiro et al., 2007). The seismicity continues for some time after shut-in as the fluid leaks off into the surrounding rock volume and disturbs the existing stress state and reactivates natural fractures and other rock fabric features. This is consistent with the analysis of Albright and Pearson (1982), Warpinski et al. (2001), and Ghassemi et al. (2013).

The conjecture is further supported by the observation that microseismic activity was initiated with a relatively small intake of 50 barrels of fluid during the stimulation stage (Stage 3, Figure 25), suggesting the initiation of a main hydraulic fracture. Subsequently, as injection continued, microseismic events accumulated as the SRV expanded through a HF-NF stimulation mechanism, as suggested by our stimulation results in Section 2. In contrast, during the circulation tests, a significantly larger intake of 1,300–1,600 barrels of fluid was required to fill the large SRV created during stimulation and trigger the onset of microseismicity.

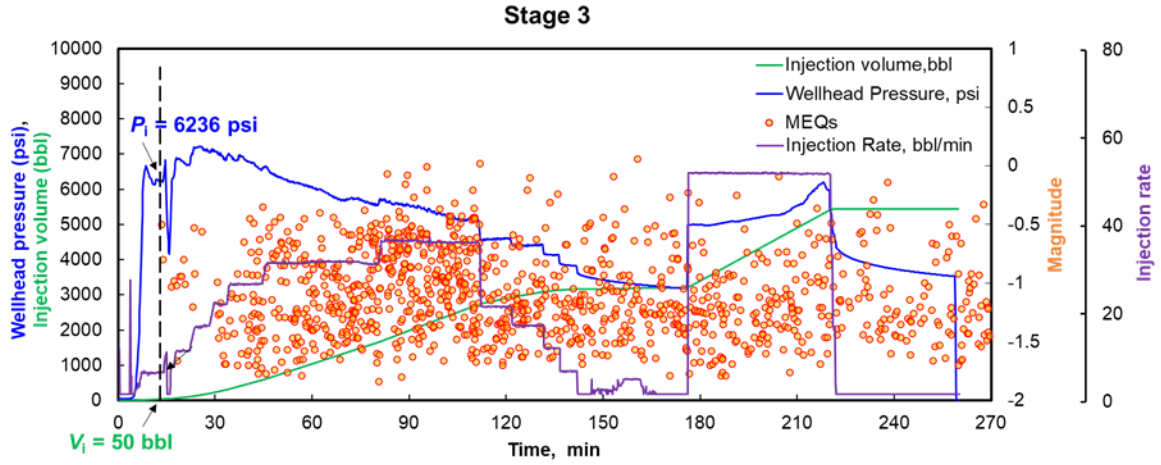

Figure 23: The temporal history of injection pressure, injection rate, total injection volume, and MEQ activities during the Stage 3 stimulation.

Different mechanisms have been called upon by Niemz et al. (2024) to explain the observed seismic activity, such as stress shadow effects and poroelastic stressing. The stress shadow due to the reopening of a hydraulic fracture and the poroelastic back stress effect can destabilize or stabilize the natural fractures near the main hydraulic fracture, depending on their location and orientation relative to the main hydraulic fracture. However, the significant pore pressure increase achieved (nearly 40-50 MPa) is highly destabilizing (Safari and Ghassemi, 2016). An estimate of the stress shadow and pore pressure perturbations can be obtained using the available data for Stage 3.

To assess the impact of poroelastic effects of pore pressure and stress, we consider both poroelastic phenomena namely, the stress induced pore pressure and the pore pressure induced stress. In doing so, we rely on the poroelastic properties of Utah FORGE rocks reported by Zhou and Ghassemi (2023) and make some simplifying assumptions about the geometry of the Stage 3 hydraulic fracture. In particular,

we assume it to be a planar circular feature of size 300 ft with constant stress and pore pressure acting on it. Assuming a planar fracture has formed at a true vertical depth of 8226 ft, the in-situ stress and pore pressure magnitudes are as follows: p=26 MPa, S_v=66 MPa, S_{Hmax}=53 MPa, S_{hmin}=45 MPa. Based on the injection pressure history of S3, the fracture propagation pressure is estimated at P_{frac}=51 MPa, yielding a high differential of 25 MPa or 3625 psi between the pressure in the hydraulic fracture and the reservoir rock mass. Assuming S_{hmin} of 45 MPa, the net pressure during circulation tests is estimated as P_{net}=51-45 or about 6 MPa or 870 psi. This net pressure would induce total stresses (stress shadow) in the vicinity of the "HF" (see Warpinski et al., 2001, for analytical calculations). As a first approximation, the mean stress shadow can be estimated as $(s_{xx}+s_{yy}+s_{zz})/3$ or $0.63P_{net}$=367 psi. This is an increase in the mean stress around the S3 hydraulic fracture (assumed to be circular) and in turn increases the pore pressure (B or Skempton's coefficient times 367 psi). Setting B=0.5, the induced pore pressure caused by the mean stress shadow is 184 psi. Then, the maximum pore pressure change in the reservoir would be 184+3625 or 3809 psi (26.3 MPa), extending to about 20 meters or 66 ft from the face of the S3 fracture. The pore pressure increase would in turn induce a poroelastic mean stress of 6.6 MPa or 953 psi (assuming a poroelastic stress coefficient of 0.25). The increase in the mean stress is likely a stabilizing force considering a maximum of 400 psi of increased differential (shearing) stress is induced (difference between induced S_{xx}, S_{yy}, S_{zz} due to shadow from analytical solution). Therefore, the increase in pore pressure by diffusion appears to be the main driver of instability for shear slip and microseismicity rather than the stress shadow. Also, cooling can also contribute to the process (Ghassemi and Zhang, 2006; Tarasov and Ghassemi, 2014; Safari and Ghassemi, 2015). The reservoir pore pressure would increase from 26 MPa to 51 MPa depending on the location with respect to the hydraulic fracture surface, while the total mean stress would increase by 1320 psi or 9.1 MPa (a net decrease in the mean effective stress from (54-26=18) to 12.1 MPa). This can potentially lead to many microseismic events due to shear (local tensile failure can occur since the pore pressure would equal or slightly exceed the S_{hmin} in the vicinity of the fracture). As a result, the delayed seismicity is likely diffusion dominated. Between C2 and C3, several days (approximately 13 days) of time have elapsed. This is sufficient for the pressure to diffuse through the rock mass. Hence when starting C3, there is a small delay between injection and the onset of MEQ. The system had to be recharged again. Accordingly, the stress relief as suggested in Segall and Lu (2015) is likely not a significant source of seismicity during C1-C4 circulations.

5. CONCLUSION

Our investigation of the Utah FORGE circulation tests has provided several key insights into the dynamics of fluid flow, rock deformation, and seismic response within the stimulated reservoir volume (SRV) in Utah FORGE. The integration of micro-seismicity data, injection pressure records, and numerical modeling has enabled a detailed analysis of the SRV's geomechanical characteristics, revealing complex interactions between hydraulic and natural fractures. Firstly, our numerical findings underscore the intricate nature of the SRV created through multi-stage stimulations (Stages 1-3), particularly highlighting the interaction between induced hydraulic fractures and pre-existing natural fractures. This interaction not only enhances the SRV's complexity but also contributes significantly to its permeability and seismic behavior. Secondly, the circulation tests between wells 16A and 16B have shown that significant fluid intake and elevated pressures are required to maintain flow within the large SRV. Notably, the seismicity associated with these tests provides a unique window into the subsurface processes, indicating a departure from the expected behavior as suggested by the Kaiser effect, where microseismic events are triggered at pressures lower than those recorded during the initial stimulation. Moreover, our analysis suggests that the orientation and characteristics of natural fractures play a pivotal role in the seismic response to fluid injection. Zones with unfavorably oriented fractures (SRVs surrounding Stages 1-2 stimulation) or high cohesion exhibit less seismic activity despite similar pressure conditions, likely due to their inability to support significant shear displacement or dilation. In conclusion, the Utah FORGE project has contributed valuable data to analyze rocks and fractures deformation, fluid flow, seismicity during EGS stimulation and fluid circulation. Our research underscores the essential need for continuous refinement of stimulation strategies to enhance geothermal energy extraction. It emphasizes the importance and the value of microseismic monitoring in characterizing fluid flow and fracture development.

ACKNOWLEDGEMENTS

This project was supported by the Utah FORGE project sponsored by the U.S. Department of Energy, through the project "Fiber-Optic Geophysical Monitoring of Reservoir Evolution at the FORGE Milford Site" and "Application of Advanced Techniques for Determination of Reservoir-Scale Stress State at Utah FORGE".

REFERENCES

Albright, J.N., Pearson, C.F., 1982. Acoustic emissions as a tool for hydraulic fracture location: Experience at the Fenton Hill Hot Dry Rock Site. Soc. Petrol. Eng. J. 22 (04), 523–530.

Cornet, F.H., Helm, J., Poitrenaud, H., Etchecopar, A., 1997. Seismic and aseismic slips induced by large-scale fluid injections. In: Talebi, S. (Ed.), Seismicity Associated with Mines, Reservoirs and Fluid Injections. In: Pageoph Topical Volumes, Birkhäuser Basel, pp. 563–583.

Ghassemi, A., and Rawal, A., Zhou, X. 2013. Rock failure and micro-seismicity around hydraulic fractures. J. Pet. Sci. and Engrg. (108), 118-127. DOI information: 10.1016/j.petrol.2013.06.005.

Ghassemi, A., and Tao, Q. 2016. Thermo-poroelastic effects on reservoir seismicity and permeability change. Geothermics Special Issue on EGS. doi:10.1016/j.geothermics.2016.02.006.

Ghassemi, A., Kumar, D. 2023. Hydraulic Fracturing in Utah FORGE. 48th Workshop on Geothermal Reservoir Engineering (pp. 1-9). Stanford.

Ghassemi, A., Tarasovs, A. and Cheng, A.D.-H. 2005. Integral equation solution of heat extraction induced thermal stress in enhanced geothermal reservoirs. Int. J. Num. & Anal. Methods in Geomechanics, 29, 829-844.

Ghassemi, A., Zhang, Q. 2006. Poro-thermoelastic response of a stationary crack using the displacement discontinuity method. ASCE J. Engineering Mechanics, 132(1), 26-33.

Jung, R. 2013. EGS — Goodbye or Back to the Future. Paper presented at the ISRM International Conference for Effective and Sustainable Hydraulic Fracturing, Brisbane, Australia

Kumar, D., Ghassemi, A. 2023. 3D Modeling and Analysis of Utah FORGE Reservoir Stimulation. Unconventional Resources Technology Conference (URTeC).

Kumar, D., Liu, B., & Ghassemi, A. (2023). 3D Modeling of the Utah Forge Reservoir Stimulation with Proppant Transport and Deposition. SPE Annual Technical Conference and Exhibition.

Lee, S. H., Ghassemi, A. 2023. Stimulation Modeling and Circulation Forecasting in the Utah FORGE Doublet " GRC Transactions, 47 (2023).

Lee, S. H., Ghassemi, A., Modeling and Analysis of Stimulation and Fluid Flow in the Utah FORGE Reservoir Proc., 48th Workshop on Geothermal Reservoir Engineering. 48th Workshop on Geothermal Reservoir Engineering Stanford University, Stanford, CA (2023)

Niemz, P., McLennan, J., Pankow, K.L., Rutledge, J., England, K. 2024. Circulation experiments at Utah FORGE: Near-surface seismic monitoring reveals fracture growth after shut-in. Geothermics, 119, 102947

Safari, R., Ghassemi, A. 2015. Three-dimensional thermo-poroelastic analysis of fracture network deformation and induced micro-seismicity in enhanced geothermal systems. Geothermics, 58, 1-14.

Segall, P., & Lu, S. (2015). Injection-induced seismicity: Poroelastic and earthquake nucleation effects. *Journal of Geophysical Research: Solid Earth*, *120*(7), 5082-5103.

Shapiro, S.A., Dinske, C. 2007. Violation of the Kaiser effect by hydraulic-fracturing-related microseismicity. J. Geophys. Eng. 4 (2007) 378–383.

Soliman, M.Y., East, L., Adams, D. 2008. Geomechanics Aspects of Multiple Fracturing of Horizontal and Vertical Wells. SPE-86992. SPE Drilling & Completion, Sept., 217-228.

Tarasov, S. and Ghassemi, A. 2014. Self-similarity and scaling of thermal shock fractures. Physical Review E 90 (1), 012403-1-6.

Warpinski, N.R., Wolhart, S.L., Wright, C.A., 2001. Analysis and Prediction of Microseismicity Induced by Hydraulic Fracturing. SPE 71649. Ann. Tech. Conf. & Exh. New Orleans, LA.

Ye, Z., Ghassemi, A. 2018. Injection-induced shear slip and permeability enhancement in granite fractures. J. Geoph. Res, Solid Earth, 123, 24 p.

Ye, Z., Ghassemi, A. 2019. Injection-Induced Propagation and Coalescence of Preexisting Fractures in Granite Under Triaxial Stress. J. Geoph. Res, Solid Earth, 124, 16 p.

Zhou, X., Ghassemi, A., 2023. Poroelastic Properties of Sierra White Granite. Rock Mechanics and Rock Engineering. RMRE.